Super harmonic nonlinear lateral vibrations of a segmented driveline incorporating a tuned damper excited by non-constant velocity joints

Michael Browne[a],*, Alan Palazzolo[b]

[a]*McLaren Performance Technologies, Texas A&M University, USA*
[b]*Mechanical Engineering, Texas A&M University, USA*

Abstract

Typical industrial vibration problem solving includes utilization of linear vibration measurement and analysis techniques. These techniques have appeared to be sufficient with most vibration problem solving requirements. This is partially due to the lack of proper identification of the nonlinear dynamic response in measured data of actual engineering systems. Therefore, as an example, a vehicle driveshaft exhibits a nonlinear super harmonic jump due to universal joint excitations. This phenomenon is partially responsible for objectionable audible noise in the vehicle. Previously documented measurements or analytical predictions of vehicle driveshaft systems do not indicate nonlinear jump as a typical vibration mode. Physical measurements of the phenomena will be provided with subsequent analysis. Second, the secondary moment exciting the driveshaft system is derived with subsequent analysis showing the harmonic and super harmonic excitations. Third, a derivation of a model incorporating the linear and nonlinear modeling of a large degree of freedom system is introduced. Finally, simulations with the derived model with the universal joint excitations will be presented showing the correlation to physical test results. Therefore, a typical automotive driveshaft system is capable of producing nonlinear response, and thus the assumption of linearity is not sufficient for design validation or problem resolution in this case.
© 2008 Elsevier Ltd. All rights reserved.

1. Background

Rotating shafts have been used in various applications to connect the power source to where the work is needed to be applied. Rotating shafts typically referred to as driveshafts or propshafts transmit torque from the engine to the driving wheels in automotive applications. This is especially true for front engine with rear wheel drive or all wheel drive vehicles. In addition, it is necessary to allow for angular misalignments along the axis of rotation. Misalignment in a vehicle is due to many factors including manufacturing tolerances, packaging constraints, suspension travel, and engine dynamic movement (pitch and roll). Non-constant velocity (universal joint or Hooke's joint), constant velocity (CV) joint, and flex couplings have been used in

*Corresponding author.

E-mail address: mbrowne@tamu.edu (M. Browne).

driveshaft vehicle applications for these reasons. The most common coupling used in driveshafts are the non-constant velocity joint. This is due to the non-constant velocity's capabilities to transfer significant torque and at up to relatively large amounts of misalignment (5°–10°).

There exists a significant amount of knowledge into the basic angular kinematics of non-constant velocity joints. The kinematic relationship produces a difference of rotational position and velocity of the output shaft relative to the input shaft. In addition, due to the change of direction of applied moment to output moment, additional moments are produced as outlined by Porat [1]. Many static or pseudo static systems have been documented with subsequent complex analysis of the joints with respect to kinematics [2,3].

More interestingly, the physical kinematic relationship produces a second order, or two times per revolution, periodic angular speed fluctuation of the output shaft in spite of the input driven at a constant rotational speed through the non-constant velocity joint [4,5]. The difference of the input and output angular speeds has been defined as the Cardin Error, outlined by Porat for general rotordynamic applications [1,6]. Therefore, the nomenclature, non-constant velocity joint is applicable. The kinematic relationship explains the increase in amplitude of the periodic fluctuations of velocity as the relative u-joint angle is increased.

There has been significant research into the effects of a single non-constant velocity joint system. Porter identified critical speed ranges resulting in large amplitude oscillations for frequencies equal to or integer multiples of the system's natural frequencies using both linear and nonlinear analysis [7,8]. In addition, Porter also predicted generation of subharmonics possible, but harmonics were deduced to be of lower amplitude, and thus less consequential [8]. More recently, Chang identified the factor of the ratio of the input and output shaft stiffness influence the torsional instability regions of Porter's single non-constant velocity joint system [9]. Asokanthan also completed analysis on torsional instabilities due to non-constant velocity joints including analysis of a 2 degree of freedom system [10–12]. These addressed the torsional response of the same model incorporating a single non-constant velocity joint system with fixed bearings.

Mazzei identified parametric instabilities including flutter due to the system torsional and lateral response produced by excitation of the non-constant velocity with applied driveshaft loading [13,14]. Desmidt furthered research into the soft support boundary conditions on the output shaft including both lateral, torsional, and coupled response of the output shaft with and with support base excitation [6,15,16]. Desmidt furthered analysis into segmented shafts including dampers and closed loop feedback to control lateral vibrations [17].

There exists limited initial research into lateral vibrations caused by u-joints. This is in spite of identification of a moment normal to a shaft caused by the non-constant velocity joint by Porat [1]. Ota completed static measurement and analysis concluding that friction of the non-constant velocity joint pins do not generate this moment, and subsequent violent lateral vibrations are possible when an even integer multiple of shaft speed corresponded with the natural frequency [18,19]. Xu concluded that either the unbalance or the misalignment excitation of a non-constant velocity joint would be amplified when the excitation frequencies or the even multiples of shaft speed are near a system natural frequency [20]. Many other authors have discovered parametric and self-excited lateral and torsional vibrations including Plaut, Iwatsubo, Kato and Desmidt [6,21–23].

Rosenberg analyzed the effects of non-constant velocity joint excitation on the critical speed of a driveshaft predicting that low torque transmission would produce mild instabilities at odd submultiples of the critical speed (first bending mode of the driveshaft) while under torque would produce even submultiples of the critical speed, decreasing in response with increased torque loading [24]. Sheu's analysis from calculation of steady-state response of a softly supported shaft system resulted in the conclusion that odd harmonics are due to shaft imbalance, and the even harmonics are due to the non-constant velocity joint friction [25].

Most of the referenced work produced analytical results, but lack significant experimental data for comparison. Earles presented experimental data with a softly supported shaft system with large universal joint misalignment angles subsequently discussing limit cycles predicting the possibility of jump type phenomena, or system oscillation hysteresis [26]. The data he presented provided only a weak support for these claims Saigo continued work into frictional influence on a cross groove CV joint, showing a harmonic jump up of vibration amplitudes as rotational speeds increase [26]. The experiments of Saigo [26] and Kato [23] are not representative of a typical automotive application of a non-constant velocity joint that utilize rollers in the non-constant velocity joints between the pins and rollers, thus eliminating the frictional moment studied, similar to that analyzed and measured by Ota [18,19]. Xu completed experiments with flexible couplings

(no non-constant velocity joint) to support his previous analysis of misalignment of shaft systems showing the effects of two times running speed vibrations due to misalignment [27]. The presented experimental data does not conclusively explain or show super harmonic nonlinear dynamic lateral vibration response including jump type phenomena due to non-constant velocity joint excitations.

The prior analytical results only focus on the torsional and moment excitations under load of the non-constant velocity joint.

This ignores no load or light loading conditions, where moments also excite the lateral natural frequencies. In addition, the prior analytical models included some significant simplifying assumptions in the derivations of the equations of motion for a representation of the shaft system with the non-constant velocity joint. Our analytical model removes these assumptions and is furthermore validated with experimental measurements taken on a commercial class automotive driveline including a non-constant velocity joint. The model is accompanied by a thorough derivation of the relevant equations. It is therefore the subject of this paper to present experimental results, derivation of the secondary moment under no torque load, derivation of a complex driveshaft model and subsequent correlation of the simulation results with the experimental results.

2. Test apparatus and experimental results

The driveshaft of consideration is a commercially available driveshaft outfitted on a current production vehicle. The driveshaft is of a two piece design incorporating a CV joint at the transmission end of the shaft and two non-constant velocity joints located in the center and rear axle end of the shaft as pictured in Fig. 1. The CV joint is of the plunging type with six balls allowing for the angular misalignment. The center bearing consists of a ball bearing supported by a diaphragm type flexible rubber bushing. The non-constant velocity joint is located just to the front of the center bearing assembly. The second non-constant velocity joint is located at the rear axle end of the driveshaft. In addition, a vibration absorber, internal tuned damper (ITD), is incorporated in the front shaft to minimize vibrations due to the first bending mode of the driveshaft.

The test bench is made up of a hydraulic motor that rotates the shaft on the transmission side, and a spindle at the opposite end to support the axle side of the driveshaft as shown in Fig. 2. Finally, a support for the center bearing is in the middle. This support was designed to adjust the height of the center bearing. This adjustment is used to test the driveshaft with different universal joint angles by changing the height of the center bearing. It is significant as the system has no brake or secondary motor to provide additional torque. Therefore, the "load" torque in the shaft system is primarily due to inertia. This fixture has the capability of testing the driveshaft through a range of speeds. The test fixture ramps the driveshaft's rotational speed up and down through a typical vehicle's speed range of operation. Data acquisition equipment records the speed and vibration response data for analysis. Rotational speed data is collected through use of a tachometer, and vibration data is measured by accelerometers located on the transmission spindle, axle spindle, center-bearing bracket, and on the center bearing.
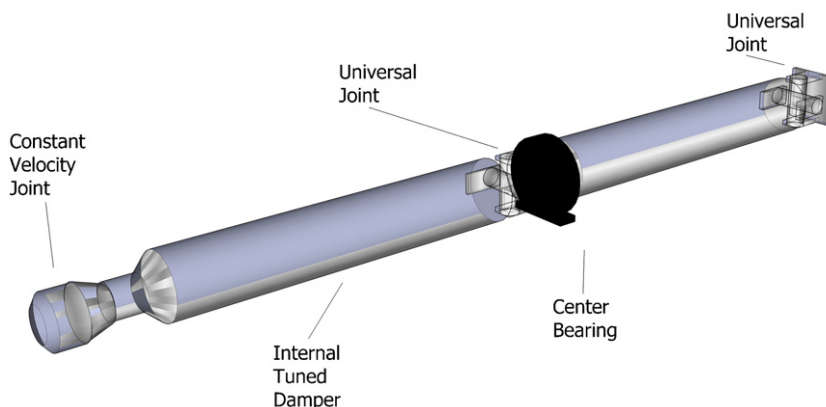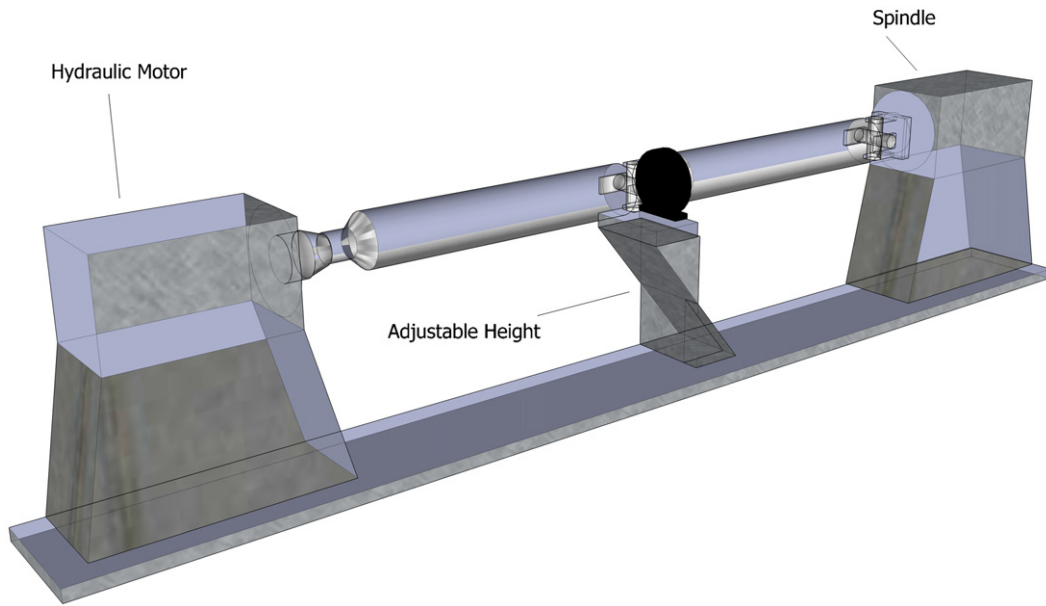

Fig. 1. Diagram of driveshaft.

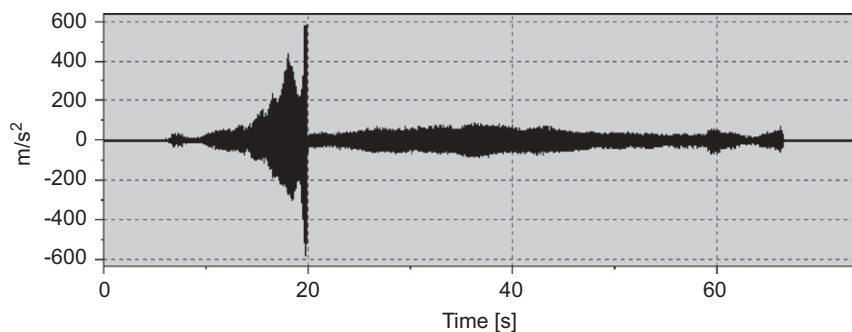Fig. 2. Diagram of driveshaft in test bench.

Fig. 3. Run-up and run-down measurement on center bearing axial direction (speed direction change at 35 s).

A non-constant velocity joint creates harmonic and super harmonic excitation on a driveshaft. The driveshaft response jumps during a ramp-up due to a nonlinearity in the systems. This response is most significant at the soft support of the center bearing of the driveshaft. Measurements of the acceleration on the soft support are presented in Figs. 3 and 4 for a run up and run down conditions ran back to back in different directions. Spectral analysis identifies the primary harmonics comprising the excitations of the jump are the fourth and eighth-order rotational. This jump follows typical stiffening nonlinear characteristics, as the jump is significant on a run up portion of a test and minimal and at a lower rev/min (frequency) during the run-down portion of the test cycle. This is significant, as complaints of noise from the fourth and eighth-order rotational harmonic exist in the vehicle application.

Measurement of the natural frequencies of the test setup will be vital to model the system correctly. An experimental modal analysis of the driveshaft in the test fixture was completed and the responses curve fitted to obtain the natural frequencies, modal damping, and the mode shapes. Standard industry practices for experimental modal analysis were completed using LMS CADA-X software for both the data acquisition and analysis. A list of the mode frequencies less than 500 Hz is presented in Table 1. These frequencies are identified as critical to creating a model that accurately represents the physical system. Therefore, the physical system's model has to have natural frequencies near these measured values and similar mode shapes.
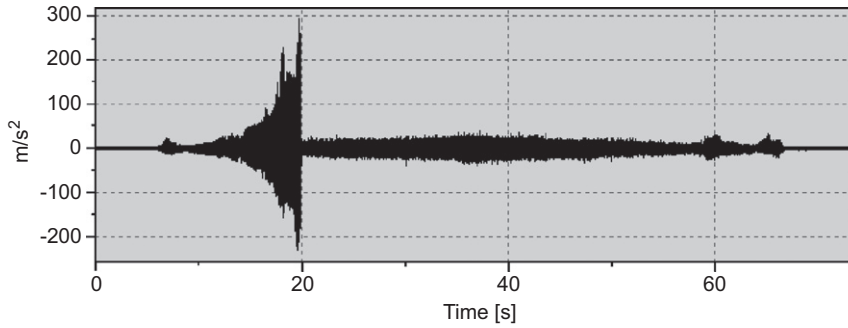
Fig. 4. Run-up and run-down measurement on center bearing vertical direction (speed direction change at 35 s).

Table 1
Experimental identification of driveshaft natural frequencies.

Mode	Natural frequencies (Hz)
Center bearing bounce	16.5
Front driveshaft/ITD lower	95
Front driveshaft/ITD upper	146
Rear driveshaft bending	162
Front driveshaft second bending	385

Additional physical measurements were necessary to identify nonlinear characteristics of components other than the universal joint. Force vs. deflection and moment vs. deflection measurements were completed on all elastomeric components in the driveshaft system including the ITD. A plot of the stiffness coefficient of the ITD, and a mathematical curve fit is presented showing a cubic and a linear dependence of force on the deflection is presented in Fig. 5. The known mass, damping, and stiffness is incorporated into a mathematical SDOF system representing the ITD by

$$0.293\ddot{x} + 1.07\dot{x} + 1.577 \times 10^5 x + 4.194 \times 10^{11} x^3 = 0, \tag{1}$$

where x is the relative displacement between the driveshaft and the ITD mass (Fig. 6). This is the case in the range of deflections shown, however the dependence transitions from hardening to softening as the displacements increase significantly. In addition, a moment vs. deflection mesurement of the center bearing also revealed nonlinear stiffness with a cubic and linear moment—deflection dependence as well, as depicted in Fig. 7. Therefore, due to multiple nonlinearities in the system, it is difficult to identify the primary source of the nonlinearity with these measurements. Results from the model and subsequent analysis determined that the ITD was responsible for the jump.

3. Analytical results

The model development consisted of two major components: a full derivation of the secondary moment with little or no torque, and the derivation of the full system model. The secondary moment derivation is included in Appendix A resulting in an equation dependent on the angular misalignment and rotational speed. The secondary moment has components in both orthogonal directions of the plane perpendicular to the rotational axis of the output shaft are

$$Ms_x = \left(-\frac{2 * I * \sin(\alpha)^3 * \cos(\omega * t)^3 * \cos(\alpha)^2 * \omega^2 * \sin(\omega * t)}{(-1 + \sin(\alpha)^2 * \cos(\omega * t)^2)^3} - \frac{\sin(\alpha) * \cos(\omega * t)^2 * \cos(\alpha) * Md}{(-1 + \sin(\alpha)^2 \cos(\omega * t)^2)} \right) \tag{2}$$
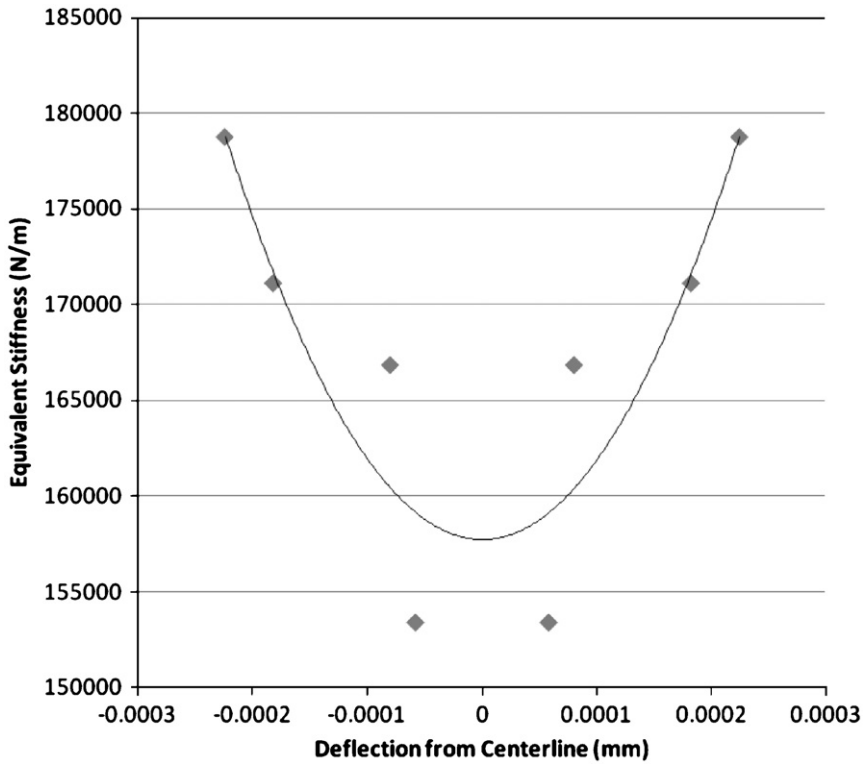
Fig. 5. Vibration absorber (internal tuned damper) stiffness and fit. ♦ Measured stiffness and — fit with: $y = 419{,}411{,}091{,}054.13x^2 + 0.00x + 157{,}742.90$, $R^2 = 0.78$.
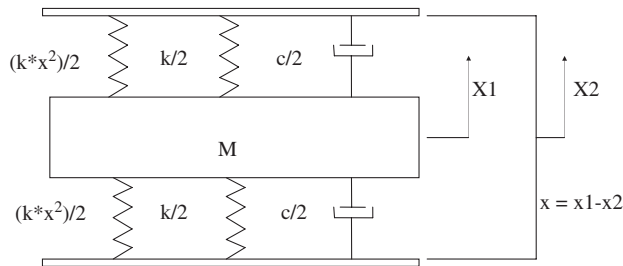

Fig. 6. Diagram of the vibration absorber (internal tuned damper) in driveshaft.

and

$$Ms_y = \left(-\frac{2 * I * \sin(\alpha)^3 * \sin(\omega * t)^2 * \cos(\omega * t)^2 * \omega^2 * \cos(\alpha)}{(-1 + \sin(\alpha)^2 * \cos(\omega * t)^2)^3} - \frac{\sin(\alpha) * \sin(\omega * t) * \cos(\omega * t) * Md}{(-1 + \sin(\alpha)^2 \cos(\omega * t)^2)} \right). \quad (3)$$

This moment is comprised of significant harmonic excitation, especially the second order in the x-direction, and fourth order in the y-direction.

3.1. Model derivation

Due to the complexity of the driveshaft system, significant work was completed in deriving a system of equations representing the physical system. A lumped mass beam element model was chosen for the FEA analysis. This lumped beam model has previously been used with good correlation results for previous work
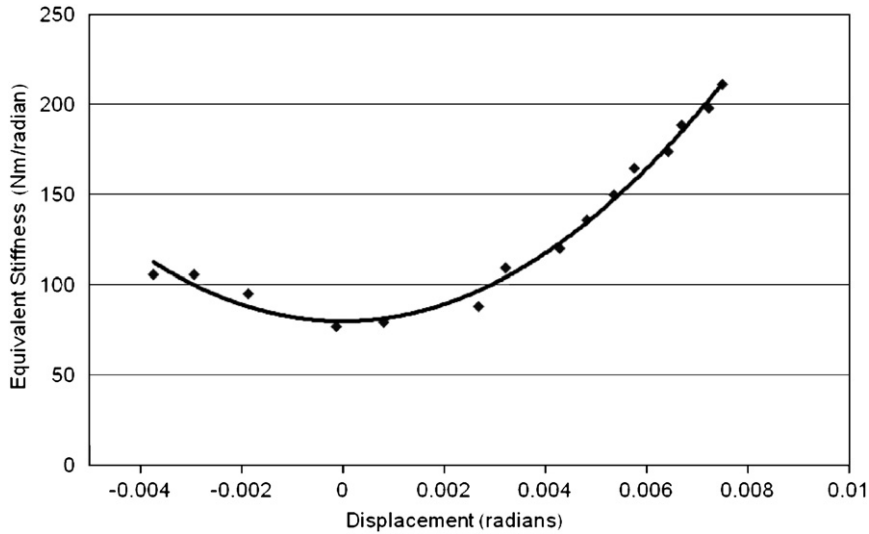
Fig. 7. Center bearing stiffness and fit. ◆ Measured stiffness and — fit with: $y = 2341339.0096103x^2 - 0.0000181x + 79.6410787$, $R^2 = 0.9874474$.
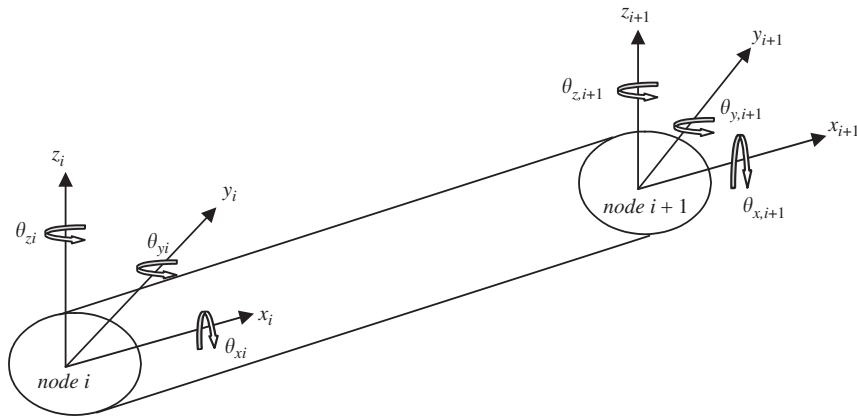

Fig. 8. Nodal degrees of freedom for a 3-D beam type finite element.

on similar driveshaft analysis. The lumped mass helps to simplify the FEA model by only having diagonal terms for the mass matrix. Therefore, the FEA model consists of massless beam elements and concentrated inertias as shown in Fig. 8. The nodal rotational and translational degrees of freedom of the 2-noded, 6 degrees of freedom per node beam element in Fig. 8 are arranged in the element displacement vector with the following convention of

$$\mathbf{U}_e = [x_i \ y_i \ z_i \ \theta_{xi} \ \theta_{yi} \ \theta_{zi} \ x_{i+1} \ y_{i+1} \ z_{i+1} \ \theta_{x,i+1} \ \theta_{y,i+1} \ \theta_{z,i+1}]^{\mathrm{T}}. \tag{4}$$

Subsequently, the diagonal lumped mass matrix and stiffness matrix for the beam element are

$$\mathbf{M}_e = \mathrm{diag}([m_i \ m_i \ m_i \ I_{p,i} \ I_{t,i} \ I_{t,i} \ m_{i+1} \ m_{i+1} \ m_{i+1} \ I_{p,i+1} \ I_{t,i+1} \ I_{t,i+1}]) \tag{5}$$

and

$$\mathbf{K}_e = \begin{bmatrix} a_1^e & 0 & 0 & 0 & 0 & 0 & -a_1^e & 0 & 0 & 0 & 0 & 0 \\ & a_2^e & 0 & 0 & 0 & a_3^e & 0 & -a_2^e & 0 & 0 & 0 & a_3^e \\ & & a_4^e & 0 & a_5^e & 0 & 0 & 0 & -a_4^e & 0 & a_5^e & 0 \\ S & & & a_6^e & 0 & 0 & 0 & 0 & 0 & -a_6^e & 0 & 0 \\ Y & & & & a_7^e & 0 & 0 & 0 & -a_5^e & 0 & a_8^e & 0 \\ & M & & & & a_9^e & 0 & -a_3^e & 0 & 0 & 0 & a_{10}^e \\ & & M & & & & a_1^e & 0 & 0 & 0 & 0 & 0 \\ & & & E & & & & a_2^e & 0 & 0 & 0 & -a_3^e \\ & & & & T & & & & a_4^e & 0 & -a_5^e & 0 \\ & & & & & R & & & & a_6^e & 0 & 0 \\ & & & & & & I & & & & a_7^e & 0 \\ & & & & & & & C & & & & a_9^e \end{bmatrix}, \qquad (6)$$

where the coefficients are defined as

$$a_1^e = E^e A^e / L_e, \quad a_2^e = 12 E^e I_{x3}^e / L_e^3, \quad a_3^e = 6 E^e I_{x3}^e / L_e^2, \quad a_4^e = 12 E^e I_{x2}^e / L_e^3,$$
$$a_5^e = -6 E^e I_{x2}^e / L_e^2, \quad a_6^e = G^e J^e / L_e, \quad a_7^e = 4 E^e I_{x2}^e / L_e, \quad a_8^e = 2 E^e I_{x2}^e / L_e, \qquad (7-15)$$
$$a_9^e = 4 E^e I_{x3}^e / L_e \quad \text{and} \quad a_{10}^e = 2 E^e I_{x3}^e / L_e.$$

Initial finite element modeling of the driveshaft with beam elements spaced along the tube, and at every major change of inner or outer diameters produces a system with 162 degrees of freedom. This model was very large and thereby needed to be significantly reduced. After a few iterations of model development, a 20 degrees of freedom system was developed. This system of equations was not sufficient to produce decent simulation results. This is due to the required small time step to get results from the system with the highest natural frequency of 44 kHz. Therefore development to simplify the system of equations to a level acceptable for simulation results was necessary.

The development of the final simplified equations of motion included many steps starting with a linear modal transformation of separate front and rear driveshaft models using the node locations depicted in Fig. 9. Modal equations of motion were calculated using standard analytical modal analysis techniques to determine natural frequencies and mode shapes. These modal equations of motions were truncated to use only the equations with the natural frequencies in the range of study, modes with natural frequencies less than 500 Hz.
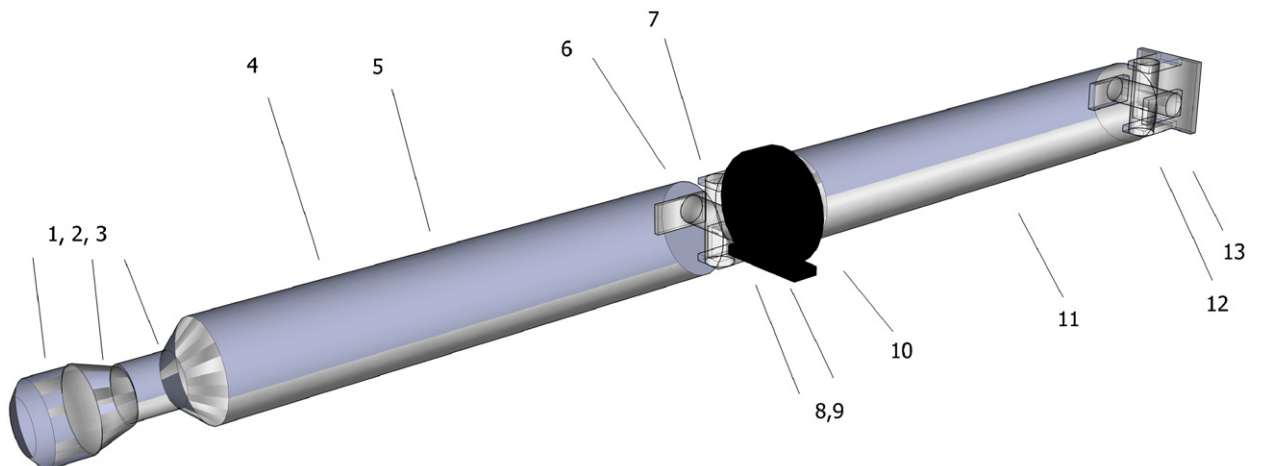

Fig. 9. Finite element model node locations.

Table 2
Comparison of analytical and experimental natural frequencies.

Mode	Normal modes	Test response (Hz)
Center bearing bounce	15.6	16.5
Front driveshaft/ITD lower	106	95
Front driveshaft/ITD upper	162	146
Rear driveshaft bending	233	162
Front driveshaft second bending	457	385

The ITD was added to the front driveshaft using an additional degree of freedom coupled to the front driveshaft modal equations of motion at the node where it is located in the driveshaft. This attachment is completed using the mode shape scaling functions necessary for physical to modal or modal to physical transformations. It is interesting to note that an additional linear stiffness and nonlinear stiffness terms were added to each modal equation of motion. Likewise, the center bearing to the rear driveshaft nonlinear stiffness was added using the same modal modification techniques. This generated nonlinear modal coordinate equations of motion for the front and rear driveshafts, respectively.

The driveshafts were then coupled together with a hinge joint using modal coupling techniques at the location of the universal joint. A standard pin couple was performed at this point. The transformation matrix was defined in the physical coordinate system, and thereby transformed using the same physical to modal transformation matrices used for the modal equations of motion derivation. This was necessary to couple the equations at this point to ensure adequate freedom of vibration across the universal joint angle.

The final system of equations had 7 degrees of freedom, with two dependant modes from the modal coupling to produce 5 modal degrees of freedom for the final simulation. Care was taken during the assembly process as the driveshafts, ITD, and universal joint forces were developed using multiple coordinate systems, and transformation into a global coordinate system was necessary. The universal joint force was added to the node where the universal joint connects the front and rear driveshaft. Once again physical to modal coordinate system transformation was necessary resulting in a forcing component in each of the equations of motion.

The final results for analytical linear model normal modes analysis (removing the nonlinear terms) and the experimental modal analysis results are presented in Table 2. The linear modal analysis and the experimental modal analysis are comparable as they both assume linearity of the equations of motion. There is good agreement of the normal mode analysis and the test response up to the frequency of the jump. The rear driveshaft bending mode has a significant discrepancy of identified natural frequencies. Upon review of the data, the rear axle spindle has a significant cantilevered overhang of the flange attachment to the universal joint flange on the driveshaft. This overhang adds flexibility that was not included in the Normal mode analysis, which includes only the driveshaft stiffness influences.

In summary, the final modal equations of motion include the nonlinear ITD stiffness, nonlinear center bearing moment stiffness, and have freedom across the universal joint angle direction. In addition, the excitation is the full function formula and includes possible parametric excitation due to the universal joint angles changing due to the vibration. The following equation presents the form of the final modal equations of motion used for the subsequent simulation analysis

$$\mathbf{M}\ddot{q} + \mathbf{C}\dot{q} + \mathbf{K}q + \mathbf{K}_{\text{cubic}}q^3 = \mathbf{F}(q, \alpha, t), \tag{16}$$

where M, C, K are the linear modal mass, damping, and stiffness matrices, K_{cubic} is the cubic stiffness, and $F(q, \alpha, t)$ is the modal forcing vector that is dependent on the modal state, misalignment angle, and time.

3.2. Simulation results

The simulation of a ramp up similar to the experiment resulted in a nonlinear jump occurring at approximately 2100 rev/min in both the ITD and the driveshaft at the location of the ITD as plotted in Fig. 10, respectively. The freedom across the universal joint connection can be seen with the responses of the front and
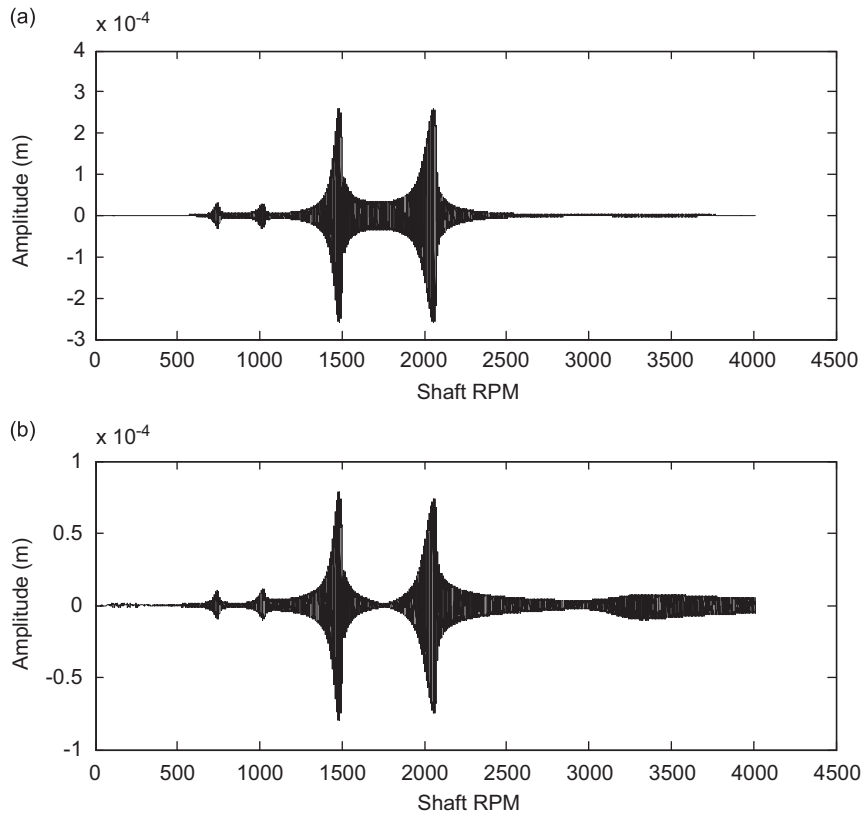
Fig. 10. Simulation results of: (a) internal tuned damper and (b) driveshaft at location of the internal tuned damper.

rear driveshaft angle response at the universal joint. This is shown Fig. 11 with each individual angle presented first, and then the difference between the angles presented in the last plot. The jump is also apparent in the universal joint angles, reflecting the front shaft in the front universal joint, but a slightly different response in the rear shaft angle. The response of the rear universal joint angle is similar in shape as the response on the center bearing x-direction lining up with the rear driveshaft, and z-direction for the front driveshaft for the fourth-order response from the experimental test results. Comparisons of the experimental results in Fig. 12 to the predicted results in Fig. 9 shows some interesting features. Two peaks are present in both results, but the experimental measurement has the peaks closer together. These results align with the small differences between the normal modes and test results of the identification of the natural frequencies, see Table 2.

Figs. 11b and 13 show a similar behavior with two peaks, and greater separation in the simulation results due to the results of the normal modes analysis. The simulation results are displacements while the measured results are acceleration. This will change the shapes of the responses but not the separations in peak amplitude speeds. The responses of the universal joints are dominated by the fourth-order excitation progressing through the range of the front shaft bending and ITD tuning frequency.

The simulation was completed with the derived full secondary moment equation and a truncated Fourier series approximation. The results showed little difference in the simulated displacements. A comparison of the results is shown in Figs. 14a and b for the full moment equation and (b) and (c) for the Fourier series equation. Either equation is sufficient for use in analysis with the same misalignment angle. The nonlinear stiffness of the ITD was removed, and the results produced a standard linear response without the jump. The linear results with inclusion of parametric excitation of the forced secondary moment due to the universal joint prove that the nonlinear ITD stiffness is responsible for the jump, and not parametric excitation or resonance. Subsequently, the experimental data presented previously in Figs. 3 and 4 with the drive up portion (0–35 s) showing a significant jump, but a subsequent jump during the run down portion (35–70 s) produced a
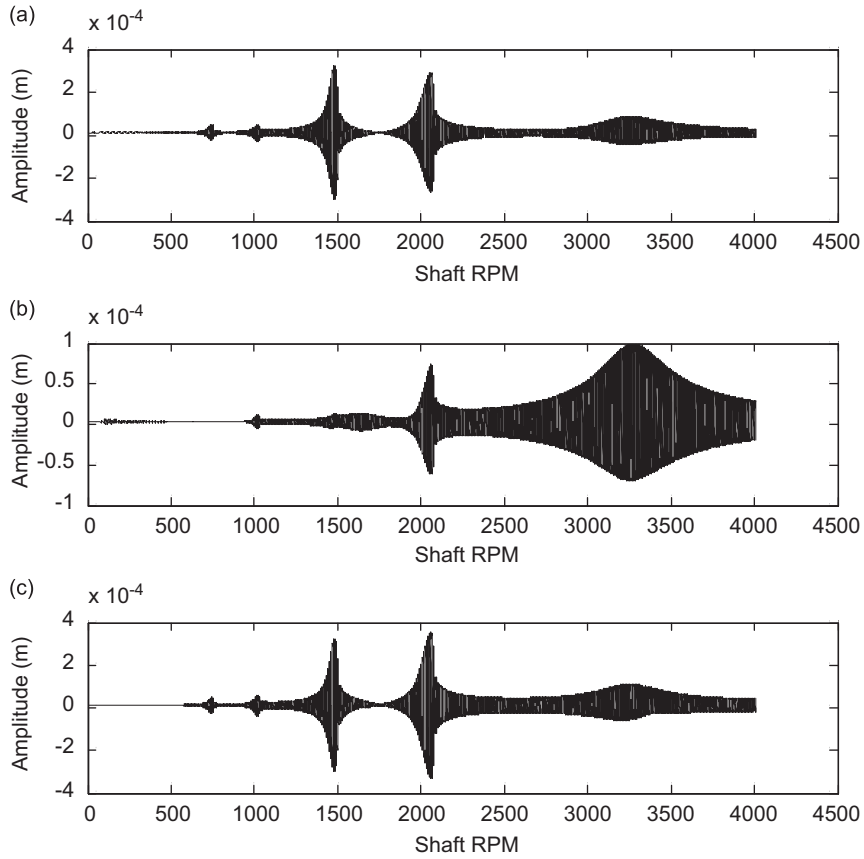
Fig. 11. Simulation results of universal joint angles: (a) front shaft angle at universal joint, (b) rear shaft angle at universal joint, and (c) angle between front and rear shafts at universal joint.
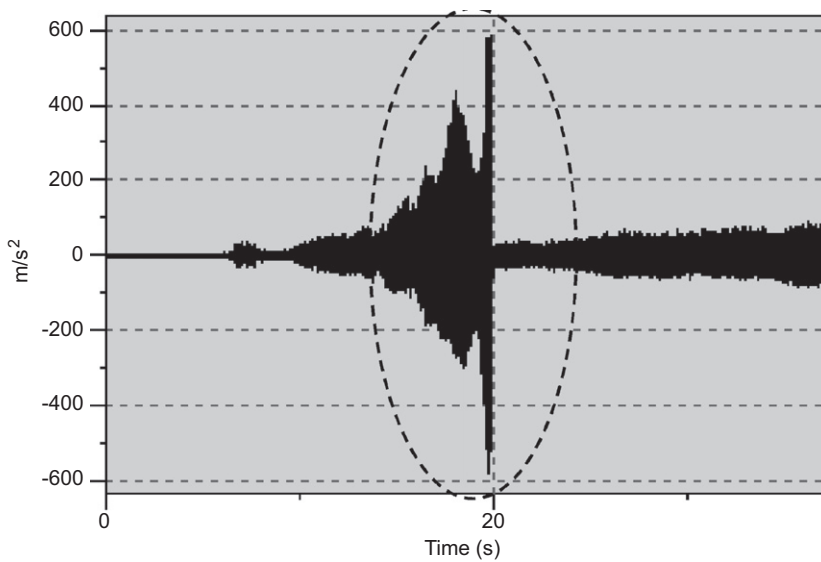

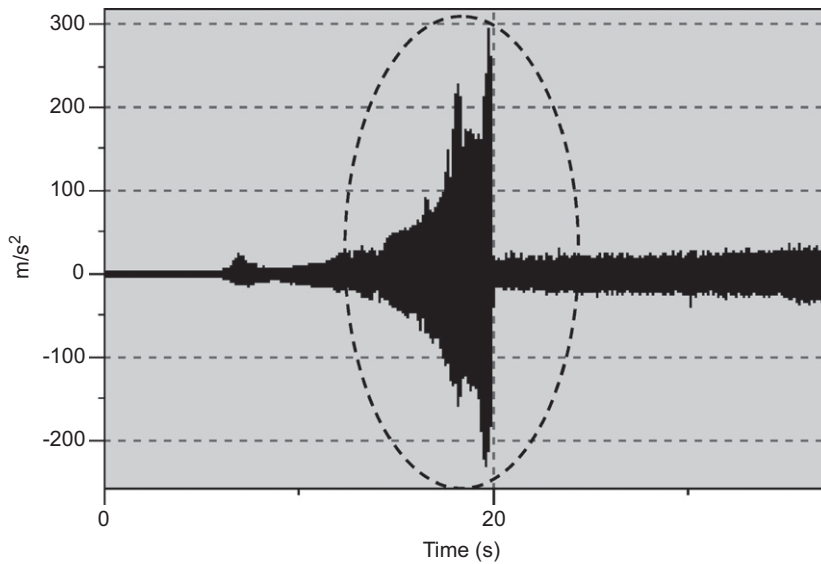Fig. 12. Fourth-order center bearing response top *X*-direction.

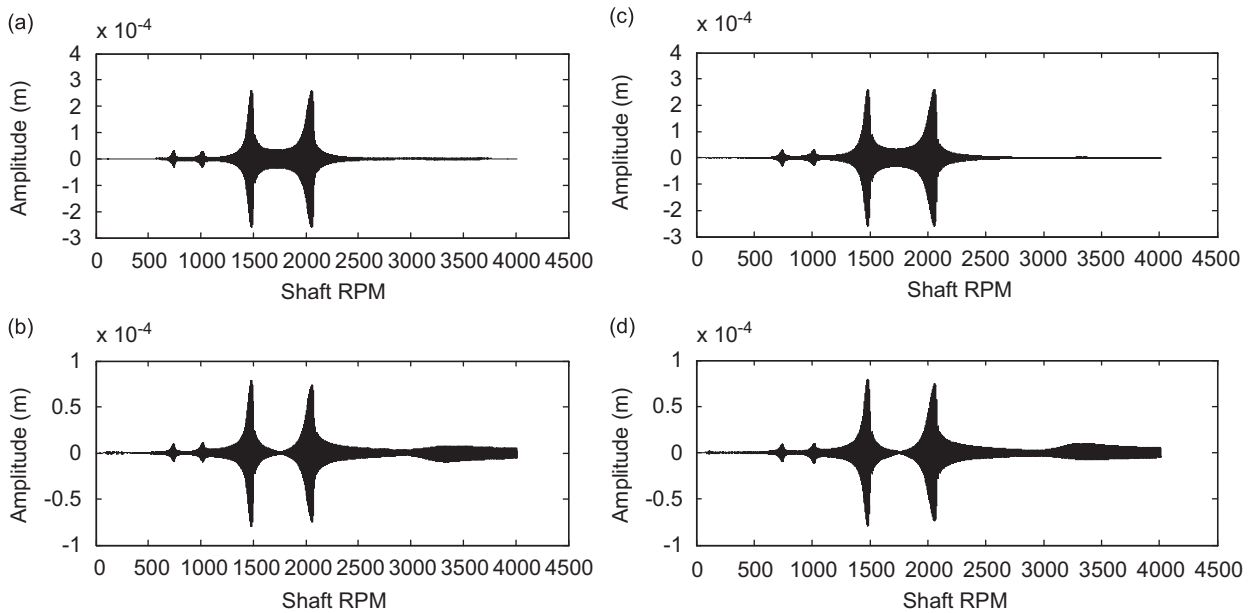Fig. 13. Fourth-order center bearing top *Z*-direction.

Fig. 14. Simulation results with full moment equation of: (a) internal tuned damper and (b) on driveshaft at location of internal tined damper. Results with Fourier series moment equation: (c) internal tuned damper and (d) on driveshaft at location of internal tined damper.

significantly different level, and response through the resonance region. This response is a symptom of nonlinear response and a parametric excitation would have similar responses in both conditions.

   Additional runs at various levels of nonlinearity were made to determine the minimum level of nonlinearity that produces a noticeable jump. This incipient level for the 4° angle case was at 25% of the measured nonlinearity of the ITD stiffness. From the force input dependency on misalignment angle, the minimum level of nonlinearity to produce a jump would vary inversely with the angle of misalignment.

4. Conclusions

Nonlinear vibration response of a common automotive driveshaft has been measured and explained by model characterization at the component and system levels, system simulation, and correlation with the test data. The physical nonlinearity was isolated to the ITD which helps to reduce unwanted vibrations due to external forces, but not due to the universal joint related excitations. These moment excitations were created by the misalignment angle producing a secondary moment as a resultant of the known geometric kinematics forcing the output shaft angle to vary from the input shaft angle. It is interesting to note that a second factor, the load inertia also influences the secondary moment. The Eqs. (2)–(3) clearly indicate that the inertia proportionally changes the secondary moment. Due to this proportional influence, the influences are similar to angle changes, with angle changes having a correlated but not proportional influence. Therefore, angle changes are a more interesting factor for studying the influence of the forced excitation level.

These results provide a basis for further analysis of the universal joint excitations and dynamic response of driveshaft systems for reducing unwanted noise and vibrations. Future work includes running similar tests with a ''4 square'' rig to investigate the effects of locked in torque, and developing a linear spring ITD that will provide good dampening effects without the nonlinear jump.

Acknowledgments

Appendix A. Derivation of the secondary moment

As outlined in reference paper [19], p and q are the orthogonal vectors of the cross pin as pictured in Fig. A1. The vectors change as a function of the input rotation angle, Ψ, or the output rotation angle, θ. These vectors are also dependent on the universal misalignment angle, α. The global coordinate system is defined as having the z-direction along the axis of rotation of the output shaft, Y in the vertical, and X in the axis parallel to the ground into the plot. This coordinate system's orientation is pictured in Fig. A2. In addition, the three angles: ψ, α, and θ are shown for the following derivation. The output shaft angle changes as a function of the input angle and the angle of misalignment by

$$\theta = \arctan\left(\frac{\tan(\psi)}{\cos(\alpha)}\right). \tag{A.1}$$

Due to the nature of the universal joint, the only moment acting on the cross pin is perpendicular to the cross pin, assuming frictionless interaction between the cross pin and the shaft yokes. This direction is mathematically defined by the cross product of vectors p and q. Assuming the magnitude of the input moment is M, then the moment on the cross pin is derived as

$$\begin{aligned}\mathbf{M} = &- M * \sin(\alpha) * \cos(\psi) * \cos(\theta)\mathbf{i} - M * \sin(\alpha) * \cos(\psi) * \sin(\theta)\mathbf{j} \\ &+ M * (\cos(\alpha) * \cos *(\psi) * \cos(\theta) + \sin(\psi) * \sin(\theta))\mathbf{k}.\end{aligned} \tag{A.2}$$

Due to the complexity of the joint, M is not known or typically measured. The output shaft moment, Mo, is known. Therefore, M can be calculated from Mo as

$$Mo = M * (\cos(\alpha) * \cos *(\psi) * \cos(\theta) + \sin(\psi) * \sin(\theta)). \tag{A.3}$$

The output shaft only has reaction moments in the axial, z-direction, due to the transmission of torque or angular acceleration of the output shaft assuming no friction between the cross and the shaft yokes. Solving for M and substituting it into Eq. (A.2) yields the vector form of the moment on the cross pin as

$$\mathbf{M} = -\frac{\sin(\alpha) * \cos(\psi) * \cos(\theta) * Mo}{(\cos(\alpha) * \cos *(\psi) * \cos(\theta) + \sin(\psi) * \sin(\theta))}\mathbf{i} - \frac{\sin(\alpha) * \cos(\psi) * \sin(\theta) * Mo}{(\cos(\alpha) * \cos *(\psi) * \cos(\theta) + \sin(\psi) * \sin(\theta))}\mathbf{j} + (Mo)\mathbf{k}. \tag{A.4}$$
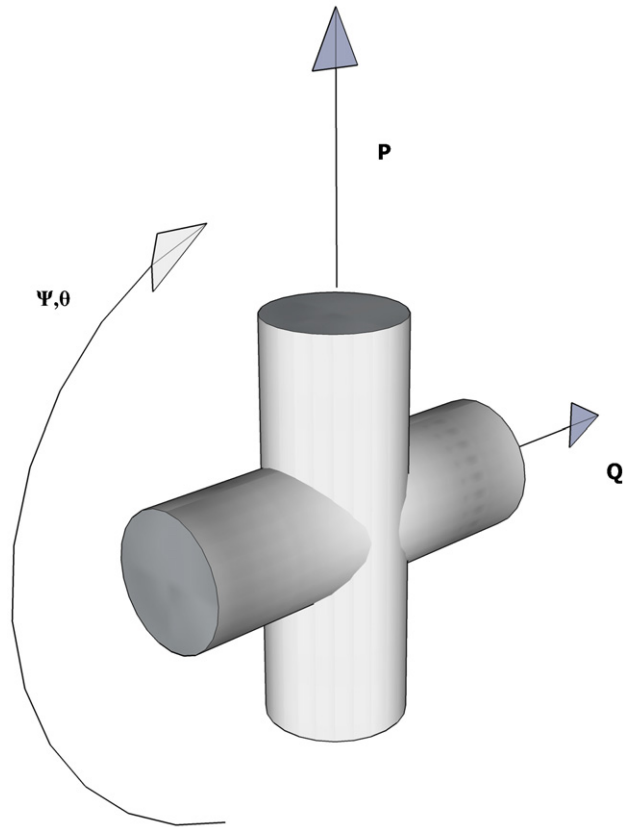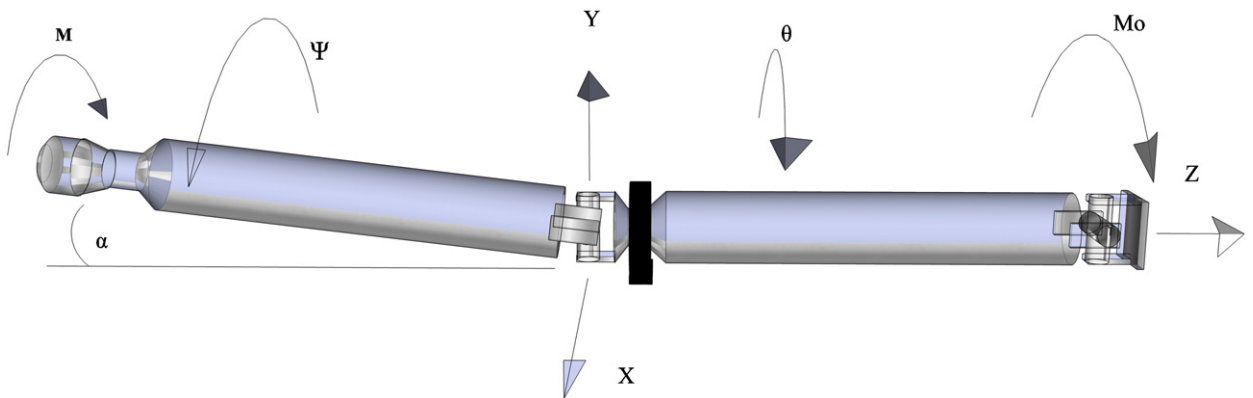
Fig. A1. Cross pin vectors.

Fig. A2. Coordinate system for secondary moment derivation.

Finally, the secondary moment, *Ms*, is defined by a moment perpendicular to the output moment, *Mo*, and also perpendicular to the direction of the cross pin connected to the rear shaft yoke direction, *q*. The magnitude of the secondary moment and its vector is defined as

$$Ms = -\frac{\sin(\alpha) * \cos(\psi) * Mo}{(\cos(\alpha) * \cos *(\psi) * \cos(\theta) + \sin(\psi) * \sin(\theta))} \tag{A.5}$$

M. Browne, A. Palazzolo / Journal of Sound and Vibration 323 (2009) 334–351

and

$$\mathbf{Ms} = -\frac{\sin(\alpha) * \cos(\psi)^2 * \cos(\alpha) * Mo}{(1 - \sin(\alpha)^2 * \cos(\psi)^2)}\mathbf{i} - \frac{\sin(\alpha) * \cos(\psi) * \sin(\psi) * Mo}{(1 - \sin(\alpha)^2 * \cos(\psi)^2)}\mathbf{j} \quad (A.6)$$

in the global coordinate system. The resultant output moment, *Mo*, is comprised of all moments applied to the rear shaft defined by

$$\sum M = I * \ddot{\theta},$$

$$Mo + Md = I * \ddot{\theta},$$

and

$$Mo = I * \ddot{\theta} - Md. \quad (A.7)$$

In this case, the total moments are the output moment and a resultant driving torque at the axle end of the driveshaft, *Md*. This assumes the rear shaft is rigid in the torsional direction, thereby having no potential or stored energy. The input angle can be defined as a function of time and the rotational speed, ω, in

$$\psi(t) = \omega * t. \quad (A.8)$$

Substituting into Eq. (A.1) and derivating once and twice produces

$$\theta(t) = \arctan\left(\frac{\tan(\omega * t)}{\cos(\alpha)}\right), \quad (A.9)$$

$$\frac{\mathrm{d}}{\mathrm{d}t}\theta(t) = \frac{\omega * \cos(\alpha)}{(1 - \sin(\alpha)^2 * \cos(\omega * t)^2)}, \quad (A.10)$$

and

$$\frac{\mathrm{d}^2}{\mathrm{d}t^2}\theta(t) = -\frac{2 * \omega^2 * \cos(\alpha) * \sin(\alpha)^2 * \cos(\omega * t) * \sin(\omega * t)}{(1 - \sin(\alpha)^2 * \cos(\omega * t)^2)^2}. \quad (A.11)$$

Substituting the acceleration term, Eq. (A.11) into Eq. (A.7) results in

$$Mo = -\frac{2 * I * \omega^2 * \cos(\alpha) * \sin(\alpha)^2 * \cos(\omega * t) * \sin(\omega * t)}{(1 - \sin(\alpha)^2 * \cos(\omega * t)^2)^2} - Md. \quad (A.12)$$

Furthermore, Eq. (A.12) can now be substituted into Eq. (A.6) to obtain the secondary moment. The secondary moments in the *x* and *y* direction are

$$Ms_x = \left(-\frac{2 * I * \sin(\alpha)^3 * \cos(\omega * t)^3 * \cos(\alpha)^2 * \omega^2 * \sin(\omega * t)}{(-1 + \sin(\alpha)^2 * \cos(\omega * t)^2)^3} - \frac{\sin(\alpha) * \cos(\omega * t)^2 * \cos(\alpha) * Md}{(-1 + \sin(\alpha)^2 \cos(\omega * t)^2)}\right) \quad (A.13)$$

and

$$Ms_y = \left(-\frac{2 * I * \sin(\alpha)^3 * \sin(\omega * t)^2 * \cos(\omega * t)^2 * \omega^2 * \cos(\alpha)}{(-1 + \sin(\alpha)^2 * \cos(\omega * t)^2)^3} - \frac{\sin(\alpha) * \sin(\omega * t) * \cos(\omega * t) * Md}{(-1 + \sin(\alpha)^2 \cos(\omega * t)^2)}\right). \quad (A.14)$$

It is interesting to comment that the moments in the *x* and *y*-directions are not equal. This is due to the misalignment was completed in one plane, but the secondary moment is not just in the plane of misalignment and in fact changes direction as the joint rotates thereby not aligning with either plane. This is an effect stemming from Eq. (A.2). Therefore with effects of the moment will influence the moments in both planes differently.

It is unclear due to their complexity as to the frequency or order content of Eqs. (A.13)–(A.14). For further analysis, it needs to be shown that the Fourier series expansion of the secondary moment also has multiple excitation orders, or harmonics of the known second-order excitation due to the universal joint. The following
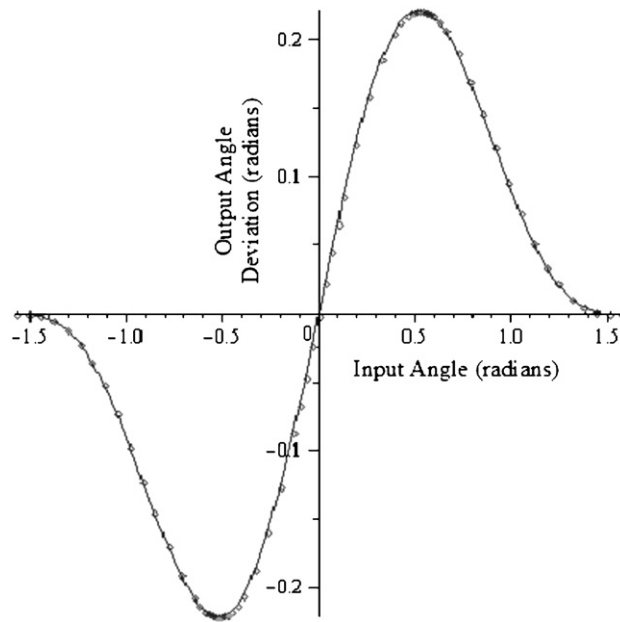
Fig. A3. Comparison plot of exact and Fourier series secondary moments.

analysis derives the, Fourier expansion for the secondary moment. The self-excitation of the universal joint is presented in the first part of the equation of both moment directions. A misalignment angle of 4° is used to simplify the equation, and is the primary angle of focus of the system's response from the physical test results. The dynamic secondary moment is presented subtracting any input load on the driveshaft, resulting in

$$Ms_x = \left(-\frac{2 * I * \sin\left(\frac{\pi}{45}\right)^3 * \cos(\psi)^3 * \cos\left(\frac{\pi}{45}\right)^2 * \omega^2 * \sin(\psi)}{\left(-1 + \sin\left(\frac{\pi}{45}\right)^2 * \cos(\psi)^2\right)^3} \right). \tag{A.15}$$

Subsequently, the Fourier series for a 4° angle is

$$Ms_x = 0.00017032 * I * \omega^2 * \sin(2 * \psi) + 0.000085770 * I * \omega^2 * \sin(4 * \psi)$$
$$+ 4.2873 * 10^{-7} * I * \omega^2 * \sin(6 * \psi) + 6.6040 * 10^{-8} * I * \omega^2 * \sin(8 * \psi). \tag{A.16}$$

Fig. A3 presents the quality of the fit of the Fourier series with respect to the original equation. The Fourier series with the first two terms was reasonably close to the four term approximation. This is also verified by comparing the coefficients of the various terms, as the first two terms are significantly larger than that of the higher order terms. For demonstration purpose only, the values of $\omega = 1$, and $I = 1000$ were used to generate Fig. A3. Therefore, it is clear that the Fourier series approximation of the x-direction self excitation comprises also of the primary even integer multiples previously presented in the angular deflection and acceleration. The y-direction derivation of the self-excitation term in Eq. (A.14) calculated without the load torque is

$$Ms_y = \left(-\frac{2 * I * \sin\left(\frac{\pi}{45}\right)^3 * \sin(\psi)^2 * \cos(\psi)^2 * \omega^2 * \cos\left(\frac{\pi}{45}\right)}{\left(-1 + \sin\left(\frac{\pi}{45}\right)^2 * \cos(\psi)^2\right)^3} \right). \tag{A.17}$$
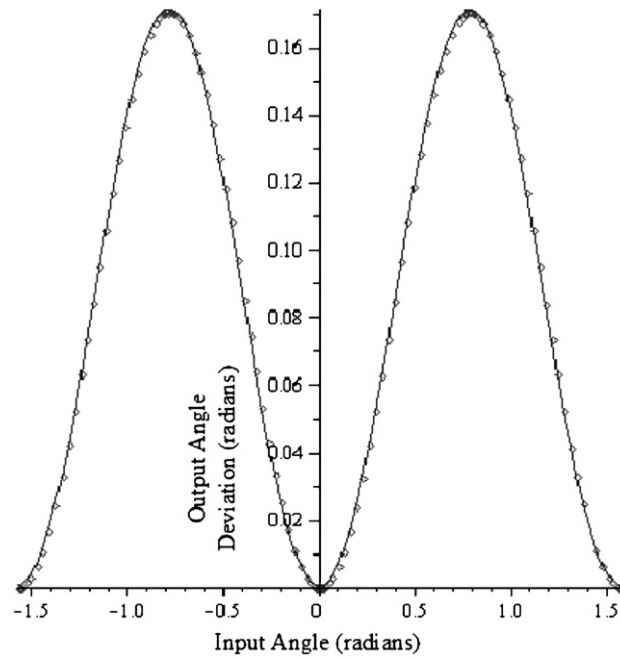
Fig. A4. Comparison plot of exact and Fourier series approximation of secondary moment.

Subsequently, the Fourier series is

$$Ms_y = 0.000085258 * I * \omega^2 + 2.8582 * 10^{-7} * I * \omega^2 * \cos(2 * \psi) - 0.000085265 * I * \omega^2 * \cos(4 * \psi)$$
$$- 3.6917 * 10^{-7} * I * \omega^2 * \cos(6 * \psi) + 8.357010 * 10^{-7} I * \omega^2 * \cos(8 * \psi). \tag{A.18}$$

Fig. A4 presents the quality of the fit of the Fourier series with respect to the original equation. Once again, the Fourier series with the first two terms was reasonably close to the four term approximation. The coefficients indicate that the fourth-order term dominates, as the coefficient is significantly larger than those of the other terms. For demonstration purpose only, the values of $\omega = 1$ and $I = 1000$ were used to generate the results plotted in Fig. A4.

References

[1] I. Porat, Moment transmission by a universal joint, *Mechanism and Machine Theory* 15 (1980) 245–254.
[2] J.E. Baker, Displacement–closure equations of the unspecialized double-Hooke's-joint linkage, *Mechanism and Machine Theory* 37 (2002) 1127–1144.
[3] I. Hostens, J. Anthonis, H. Ramon, New design for a 6 dof vibration simulator with improved reliability and performance, *Mechanical Systems and Signal Processing* 19 (2005) 105–122.
[4] E.R. Wagner, C.E. Cooney, Section 3.1.1 Cardan of Hooke universal joint, *The Society of Automotive Engineers: Universal Joint and Driveshaft Design Manual*, Vol. 7, 1979, pp. 39–76.
[5] A.H. Berker, Appendix K, Basic mathematics for Cardan universal joint problems, *The Society of Automotive Engineers Universal Joint and Driveshaft Design Manual*, Vol. 7, 1979, pp. 407–409.
[6] H.A. Desmidt, K.W. Wang, E.C. Smith, Coupled torsional-lateral stability of a shaft–disk system driven through a universal joint, *Journal of Applied Mechanics* 69 (2002) 261–273.
[7] B. Porter, A theoretical analysis of the torsional oscillation of a system incorporating a Hooke's joint, *Journal of Mechanical Engineering Science* 3 (1961) 324–329.
[8] B. Porter, Non-linear torsional oscillation of a two-degree-of-freedom system incorporating a Hooke joint, *Proceedings of the Royal Society of London. Series A, Mathematical and Physical Sciences*, Vol. 277, 1964, pp. 92–106.
[9] S.I. Chang, Torsional instabilities and non-linear oscillation of a system incorporating a Hooke's joint, *Journal of Sound and Vibration* 229 (2000) 993–1002.

[10] S.F. Asokanthan, P.A. Meehan, Non-linear vibration of a torsional system driven by a Hooke's joint, *Journal of Sound and Vibration* 233 (2000) 297–310.

[11] S.F. Asokanthan, M.-C. Hwang, Torsional instabilities in a system incorporating a Hooke's joint, *Journal of Vibration and Acoustics* 118 (1996) 368–374.

[12] S.F. Asokanthan, X.-H. Wang, Characterization of torsional instabilities in a Hooke's Joint driven system via maximal Lyapunov exponents, *Journal of Sound and Vibration* 194 (1996) 83–91.

[13] A.J. Mazzei Jr., R.A. Scott, Principal parametric resonance zones of a rotating rigid shaft driven through a universal joint, *Journal of Sound and Vibration* 244 (2001) 555–562.

[14] A.J. Mazzei Jr., A. Argento, R.A. Scott, Dynamic stability of a rotating shaft driven through a universal joint, *Journal of Sound and Vibration* 222 (1999) 19–47.

[15] M.F. Dimentberg, Transverse vibrations of rotating shafts: probability density and first-passage time of whirl radius, *International Journal of Non-linear Mechanics* 40 (2005) 1263–1267.

[16] M.F. Dimentberg, Random vibrations of a rotating shaft with non-linear damping, *International Journal of Non-linear Mechanics* 40 (2005) 711–713.

[17] H.A. Desmidt, K.W. Wang, E.C. Smith, A.J. Provenza, On the robust stability of segmented driveshafts with active magnetic bearing control, *Journal of Vibration and Control* 11 (2005) 317–329.

[18] H. Ota, M. Kato, Even multiple vibrations of a rotating shaft due to secondary moment of a universal joint, *Institution of Mechanical Engineers Conference Publications*, 1984, pp. 199–204.

[19] H. Ota, M. Kato, Lateral vibrations of a rotating shaft driven by a universal joint (1st Report, Generation of even multiple vibrations by secondary moment), *Bulletin of JSME* 27 (1984) 2002–2007.

[20] M. Xu, R.D. Marangoni, Vibration analysis of a motor-flexible coupling-rotor system subject to misalignment and unbalance, part I: theoretical model and analysis, *Journal of Sound and Vibration* 176 (1994) 379–633.

[21] R.H. Plaut, J. Wauer, Parametric, external and combination resonances in coupled flexural and torsional oscillations of an unbalanced rotating shaft, *Journal of Sound and Vibration* 183 (1995) 889–897.

[22] T. Iwatsubo, M. Saigo, Transverse vibration of a rotor system driven by a Cardan joint, *Journal of Sound and Vibration* 95 (1984) 9–18.

[23] M. Kato, H. Ota, Lateral excitation of a rotating shaft driven by a universal joint with friction, *Journal of Vibration and Acoustics* 112 (1990) 298–303.

[24] R.M. Rosenberg, On the dynamical behavior of rotating shafts driven by universal (Hooke) coupling, *Journal of Applied Mechanics* 25 (1958) 47–51.

[25] P.-P. Sheu, W.-H. Chieng, A.-C. Lee, Modeling and analysis of the intermediate shaft between two universal joints, *Journal of Vibration and Acoustics* 118 (1996) 88–99.

[26] M. Saigo, Y. Okada, Y. Ono, Self-excited vibration caused by internal friction in universal joints and its stabilizing method, *Journal of Vibration and Acoustics* 119 (1997) 221–229.

[27] J. Xu, R.D. Marangoni, Vibration analysis of a motor-flexible coupling–rotor system subject to misalignment and unbalance, part II: experimental validation, *Journal of Sound and Vibration* 176 (1994) 681–691.